Enhancing the Performance of Wide-Bandgap Polymer-Based Organic Solar Cells through Silver Nanorod Integration

ACS OMEGA

Open Access

http://pubs.acs.org/journal/acsodf

Article

Enhancing the Performance of Wide-Bandgap Polymer-Based Organic Solar Cells through Silver Nanorod Integration

Alemayehu G. Waketola,* Fekadu G. Hone, Fikadu T. Geldasa, Zewdneh Genene, Wendimagegn Mammo, and Newayemedhin A. Tegegne*

Cite This: *ACS Omega* 2024, 9, 8082−8091

Read Online

ACCESS | Metrics & More | Article Recommendations

ABSTRACT: Light trapping induced by the introduction of metallic nanoparticles has been shown to improve photo absorption in organic solar cells (OSCs). Researchers in the fields of plasmonics and organic photovoltaics work together to boost sunlight absorption and photon−electron interactions in order to improve device performance. In this contribution, an inverted OSC was fabricated by using indacenodithieno[3,2-*b*]thiophene-*alt*-2,2′-bithiazole (**PIDTT-BTz**) as a wide-band gap donor copolymer and (6,6)-phenyl-C_{71}-butyric acid methyl ester ($PC_{71}BM$) as an acceptor. Silver nanorods (Ag-NRs), synthesized by precipitation method, were embedded in the active layer of the solar cell. The device fabricated with 1 wt % Ag-NRs in the active layer showed a 26% improvement in power conversion efficiency (PCE) when exposed to 100 mW/cm^2 simulated solar illumination. The role of Ag-NRs in the performance improvement of the OSCs was analyzed systematically using morphological, electrical, and optical characterization methods. The light trapping and exciton generation were improved due to the localized surface plasmon resonance (LSPR) activated in Ag-NRs in the form of longitudinal and transverse modes. The photoactive layers (**PIDTT-BTz**:$PC_{71}BM$) with the incorporation of 0.5 and 1 wt % Ag-NR showed increased absorption, while the absorption with 1.5 wt % Ag-NRs appeared to be reduced in the wavelength range from 400 to 580 nm. Ag-NRs play a favorable role in exciton photogeneration and dissociation due to the two LSPR modes generated by the Ag-NRs. In the optimized device, the short-circuit current density (J_{SC}) increased from 11.92 to 14.25 mA/cm^2, resulting in an increase in the PCE from 3.94 to 4.93%, which is attributed to the improved light-trapping by LSPR using Ag-NRs.

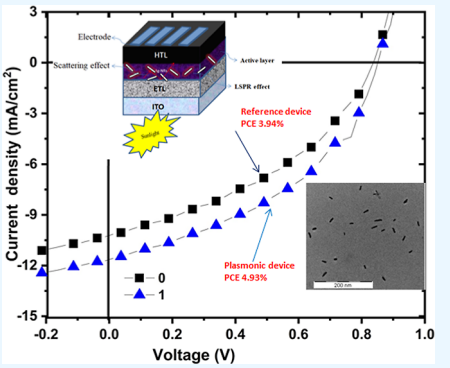

INTRODUCTION

Organic solar cells (OSCs) have attracted a lot of interest due to their lightweight, mechanical flexibility, and straightforward production method.[1−4] Intense research in materials synthesis, device fabrication, and characterization in the last 25 years has resulted in the attainment of a power conversion efficiency (PCE) of more than 19% in binary bulk-heterojunction (BHJ) OSC devices.[5] The performance of a solar cell depends on the ability of the active layer to absorb incident light, the efficiency of exciton dissociation, and the formation of charge carriers.[6] Compared with that in inorganic solar cells, light absorption in OSCs is comparatively poor because of the low carrier mobilities of organic semiconductors. Thus, the active layers in the OSCs are typically thin to ensure good carrier transport. An important limitation of OSCs is, therefore, the trade-off between light absorption and photogenerated carrier collection. The development of novel light-trapping strategies for thin-film OSC devices is an existential challenge. As a result, various light-harvesting techniques have been developed to increase the absorption of thin active layers.[7] For example, plasmonic nanoparticles (PNPs) can significantly improve light-trapping mechanisms through scattering and local field enhancement, as well as focusing the nonabsorbed frequencies of the solar spectrum into the areas of maximum absorption by absorber layers.[8] An emerging method to enhance light absorption in thin-film OSCs is the use of localized surface plasmons (LSPs) through the incorporation of metallic nanostructures. LSPs are collective oscillations of conduction electrons at the interface between the metal and dielectric material (Figure 1),[9] which upon excitation by an electric field (light) at the resonant wavelength result in strong light scattering and local electromagnetic field enhancement. An important factor affecting the plasmonic effect of metallic NPs is their morphology. Trendafilov *et al.*[10] compared octahedral-shaped silver NPs (Ag-NPs) with spherical Ag-NPs in order to study their plasmonic effect. The octahedral NPs exhibited a higher field enhancement and a larger red shift of the response

Received: October 24, 2023
Revised: January 15, 2024
Accepted: January 17, 2024
Published: February 6, 2024

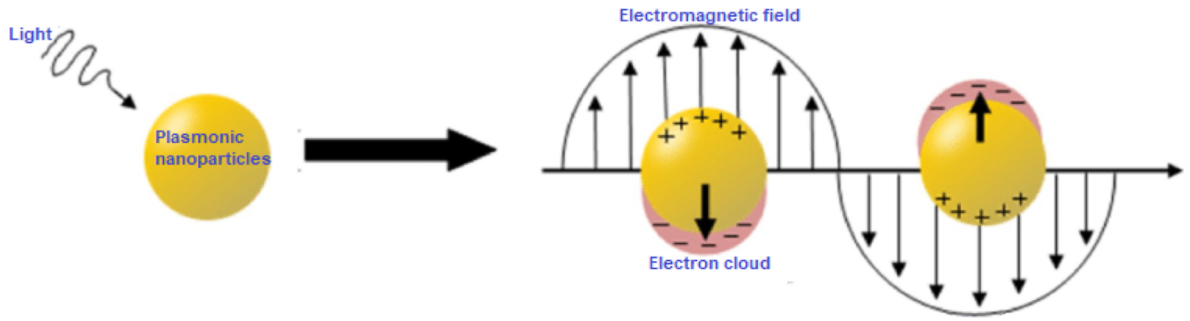

Figure 1. Schematic representation of conduction electrons oscillating across gold NPs in an electromagnetic field of incident light.

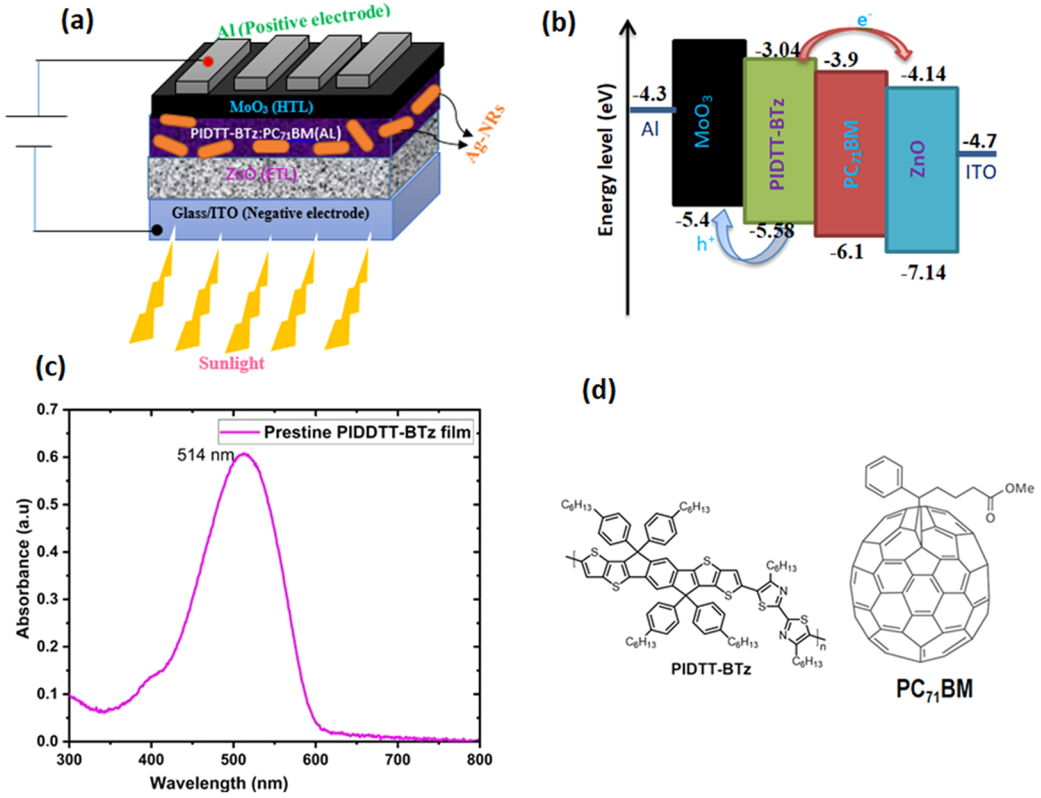

Figure 2. (a) Structure of an inverted OSC device, (b) schematic energy level diagram of materials used for device fabrication, (c) extinction spectrum of the pristine **PIDTT-BTz** polymer film, and (d) structures of **PIDTT-BTz** and $PC_{71}BM$.

than that of the spherical NPs, which are responsible for the trapping of light by solar cell devices. Silver nanorods (Ag-NRs) have been shown to have two plasmon peak positions corresponding to transverse surface plasmon resonance and longitudinal surface plasmon resonance (LSPR) at 428 and 575 nm, respectively.[11] Hsiao *et al.*[12] compared the scattering and LSPR effects of gold nanospheres (Au-NSs) and gold nanorods (Au-NRs). Thus, Au-NSs and Au-NRs were embedded in poly(3,4-ethylenedioxythiophene) polystyrene-sulfonate (PEDOT:PSS) to enhance the photon-harvesting ability of poly(3-hexylthiophene) (P3HT)-based solar cells. A solar cell fabricated with Au-NRs embedded in PEDOT:PSS demonstrated a 24% improvement in PCE, which was attributed to two LSPR absorption peaks of Au-NRs tailored to cover the absorption band edge of the active layer, thus improving light harvesting. Au-NPs have also been incorporated into the active layer of P3HT:PCBM-based OSCs to enhance device PCE from 2.6 to 3.7%, credited to the LSPR and scattering effects induced by the Au NPs.[13]

Typical conjugated polymers with wide bandgaps have low absorption due to their narrow absorption bands. These wide-bandgap polymers have absorption spectra that match the resonance of PNPs, allowing easy plasmonic amplification.[14] It is of great interest to systematically explore the impact of NPs on the performance of OSCs based on wide-bandgap polymers through their integration into the active layers. Due to their simple structure, low cost, and electron-poor nature, bithiazole-based monomers have been used to develop donor−acceptor (D−A) wide-bandgap polymers for high-performance OSCs.[15,16] Recently, a wide-bandgap D−A polymer (**PIDTT-BTz**), based on indacenodithieno[3,2-*b*]thiophene (**IDTT**) as the donor moiety and 2,2′-bithiazole (BTz) as the acceptor moiety, was synthesized and characterized by our group.[17] The polymer exhibited a narrow absorption between 400 and 600 nm with an absorption maximum of 514 nm (Figure 2c) and a PCE of 3.96% in OSC devices when blended with (6,6)-phenyl-C_{71}-butyric acid methyl ester ($PC_{71}BM$).[17] Since the absorption maximum of **PIDTT-BTz** agrees well

https://doi.org/10.1021/acsomega.3c08386
ACS Omega 2024, 9, 8082−8091

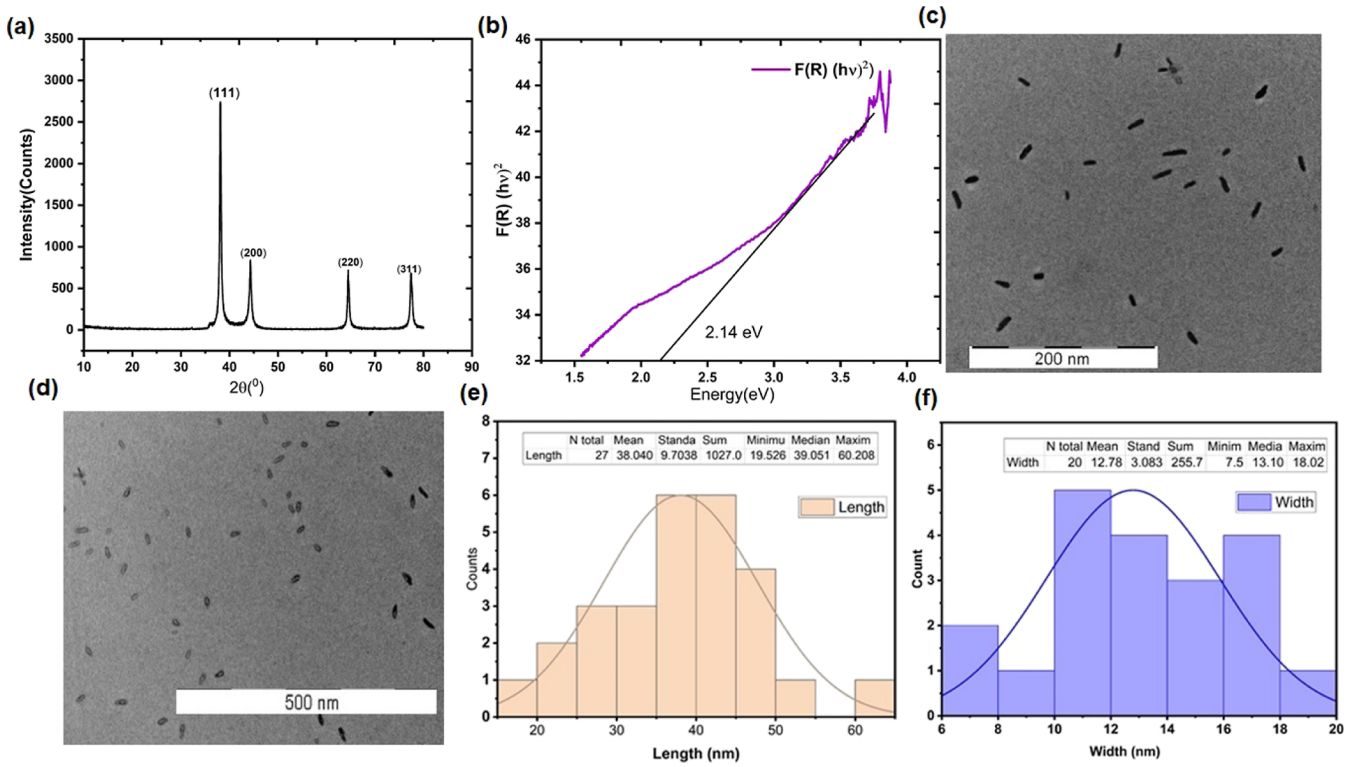

Figure 3. (a) DRS spectra of Ag-NRs; (b) XRD of Ag-NRs; (c,d) TEM image of the Ag-NRs with different scales of magnification; and (e,f) histogram of Ag-NRs for the size distribution (length and width, respectively).

with the resonance of Ag-NPs (390−520 nm),[18] its absorption can be enhanced by using such NPs, resulting in absorption coupling and then improving charge generation in the resulting OSC devices.

In this study, the performances of **PIDTT-BTz**:$PC_{71}BM$-based inverted OSC devices were investigated by embedding different amounts (0, 0.5, 1, and 1.5 wt %) of plasmonic Ag-NRs in the active layer. The influence of Ag-NRs on the morphology, charge dissociation, transport, and recombination of the devices was thoroughly examined. The device containing 1 wt % Ag-NRs showed an improvement in PCE from 3.94 to 4.93%. The plasmonic Ag-NRs contribute to the PCE enhancement mainly through scattering and local field enhancement due to longitudinal and transverse modes.

EXPERIMENTAL SECTION

Chemicals and Materials. Glass substrates precoated with indium tin oxide (ITO) with a sheet resistance of 8−12 Ω/square and exhibiting an optical transmittance of 83% at the wavelength of 550 nm were purchased from Ossila. 1,2-Dichlorobenzene (*o*-DCB), $PC_{71}BM$, and MoO_3 were purchased from Sigma-Aldrich. We reported the synthesis of **PIDTT-BTz** earlier.[17] The chemicals used to synthesize zinc oxide (ZnO) for the electron transport layer (ETL) and Ag-NRs such as 2-methoxyethanol, ethanolamine, zinc acetate dihydrate ($Zn(CH_3COO)_2{\cdot}2H_2O$), trisodium citrate dihydrate ($C_6H_5Na_3O_7{\cdot}2H_2O$), sodium borohydride ($NaBH_4$), silver nitrate ($AgNO_3$), sodium hydroxide (NaOH), and poly(vinyl alcohol) (PVA) were also purchased from Sigma-Aldrich and used as received.

Synthesis of Ag-NRs and ZnO ETL. Ag-NPs were synthesized by using coprecipitation methods. Silver nitrate ($AgNO_3$), sodium borohydride ($NaBH_4$), PVA, trisodium citrate dehydrate ($C_6H_5Na_3O_7{\cdot}2H_2O$), and sodium hydroxide of NaOH (0.92 M) were used as reactive chemicals in the present study. The precursor solutions were made in deionized water with a resistivity of 16.2 Ω cm, and all the chemicals and reagents were used as purchased without any further purifications. After many trials, the key synthesis parameters, including pH, temperature, precursor concentrations, etc., were optimized. In a 500 mL Erlenmeyer flask containing 100 mL of distilled water, 40 mL of a 0.47 M solution of $AgNO_3$ was added. The solution was stirred at room temperature, and 20 mL of a 2 wt % PVA solution was added, followed by slow addition of 8 mL of trisodium citrate dehydrate and 0.2 mL of H_2O_2 (0.012 M). The prepared solution was initially colorless; then, it changed to dark brown gradually, while 7.2 mL of a 1.44 M solution of $NaBH_4$ was carefully added to the mixture. The pH of the solution was then adjusted to 5.5 by adding the proper amount of NaOH (0.92 M). The temperature was then allowed to rise to 75 °C, and stirring continued for 1 h. The solution was then allowed to cool to room temperature, and the dark gray precipitate was collected by filtration and washed with distilled water and ethanol. Finally, the dark gray solid was dried in an oven at 80 °C for 2 h. The ZnO used as an ETL was synthesized by adopting the procedure reported by Bhoomanee *et al.*,[19] with some modifications. Thus, zinc acetate dihydrate ($Zn(CH_3COO)_2{\cdot}2H_2O$) (0.3529 g) was dissolved in a mixture of 2-methoxyethanol with an equivalent molar ratio and 90 μL of ethanolamine to prepare a 0.52 M precursor solution stirred at 60 °C for 2 h and then kept at room temperature overnight to form a clear homogeneous solution.

OSC Fabrication. Figure 2a shows a schematic diagram of the inverted solar cell devices used in this study composed of the ITO cathode layer, ZnO ETL, **PIDTT-BTz**:$PC_{71}BM$

https://doi.org/10.1021/acsomega.3c08386
ACS Omega 2024, 9, 8082−8091

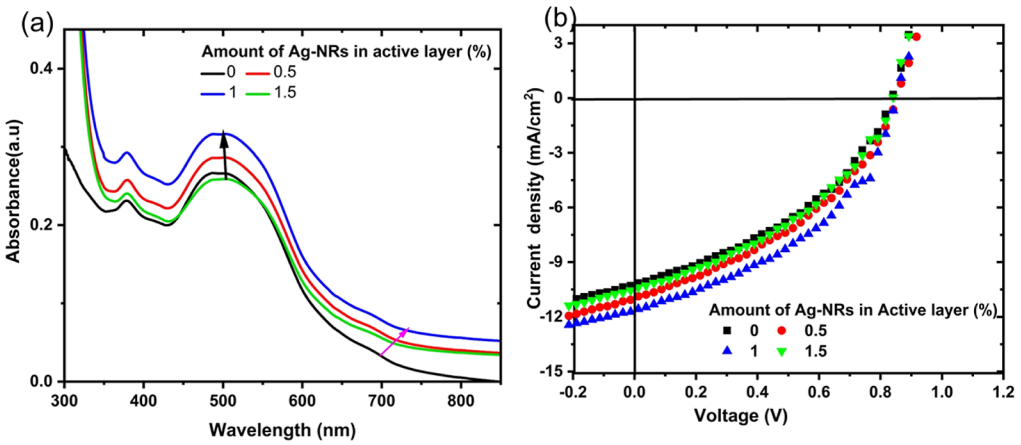

Figure 4. (a) UV−Vis absorption spectra of the active layers (**PIDTT-BTz**:$PC_{71}BM$) without and with different concentrations of Ag-NRs. (b) *I*−*V* characteristics of devices made from the active layer embedded with different concentrations of Ag-NRs.

incorporating the Ag-NR active layer, molybdenum oxide (MoO_3) hole transport layer (HTL), and aluminum (Al) anode electrode. The energy level diagram of the materials used to fabricate the solar cell devices is depicted in Figure 2b. The ZnO layer was spin-coated onto the ITO at 3000 rpm for 60 s and then annealed at 150 °C for 60 min. To prepare the OSC active layer, a 25 mg/mL solution of **PIDTT-BTz**:$PC_{71}BM$ (1:3) in *o*-DCB was stirred overnight at 60 °C. Next, to prepare an active layer with Ag-NRs, the **PIDTT-BTz**:$PC_{71}BM$ solution was weighed separately, the Ag-NR powder was added to it with weight percentages of 0, 0.5, 1, and 1.5%, and then it was evenly dispersed for 20 min by stirring at room temperature before spin-coating onto the ZnO layer and annealing at 100 °C for 10 min. In the next step, the HTL (MoO_3) was deposited by thermal deposition. The aluminum anode (150 nm) was deposited on top by evaporation. The area of all fabricated solar cell devices was 0.07 cm^2.

Characterizations. The diffusive reflectance spectra (DRS) of the Ag-NR powder were measured using a UV−visible spectrophotometer (Shimadzu, UV-1650 PC), and the absorbance spectra of **PIDTT-BTz**:$PC_{71}BM$ thin films (between 300 and 800 nm) were measured with a DS5 UV−vis spectrophotometer at room temperature. The steady-state photoluminescence spectra of active-layer thin films were measured using a HORIBA FLUROMAX-4 spectrofluorometer. Shimadzu Lab XRD-6100 was used to measure the X-ray powder diffractograms of synthesized Ag-NPs (CuKα = 1.5418 nm) at a scan speed of 3.00°/min, voltage of 40 kV, current of 30 mA, and scanning range of 10 to 80°. Transmission electron microscopy (TEM) images of the Ag-NRs and thin films were measured by a field emission transmission electron microscopy model JEOL JEM-2100F. The *J*−*V* characteristics of the fabricated solar cell devices were measured under 100 mW/cm^2 simulated solar radiation using a computer-interfaced Keithley HP2400 source meter and a Photo Emission Tech., Inc., solar simulator (model SS50AAA-EM). The Raman spectra of pristine and Ag-NR-embedded active layers were measured by using a Jobin Yvon, Horiba$^{(C)}$ TX64000 Raman spectrometer.

RESULTS AND DISCUSSION

Optical and Morphological Characterization of Ag-NRs. Figure 3a shows the X-ray diffraction (XRD) traces of the synthesized NPs, which reveal peaks at 2θ values of 38.12, 44.32, 64.48, and 77.40° corresponding to (hkl) values of the (111), (200), (220), and (311) planes of silver, respectively, according to the Joint Committee on Powder Diffraction Standards (JCPDS) card No. 04−0783. The Ag-NPs thus crystallized in face-centered cubic structures with a crystallite size of 21 nm. The optical bandgap of the Ag-NRs was determined to be 2.14 eV from the DRS spectrum given in Figure 3b using a Tauc plot of $(\alpha h\nu)^2$ *vs* photon energy (eV), where h is Planck's constant, ν is the photon frequency, and α is the absorption coefficient. The pure Ag-NPs with a wide bandgap value could find use in advanced optoelectronic devices.[18] Furthermore, the size and shape of newly synthesized Ag-NRs were characterized by using TEM, as shown in Figure 3c,d. The TEM images reveal that the synthesized Ag-NPs have a rod-like (Ag-NR) shape with an average length of 38 nm and a width of 13 nm, as obtained from the distributions given in Figure 3e,f.

Optical Absorption of Active Layers. The effect of incorporating various amounts of Ag-NRs on the optical characteristics of the reference photoactive layer (**PIDTT-BTz**:$PC_{71}BM$ (1:3)) was studied using UV−vis absorption spectroscopy, as shown in Figure 4a. Upon embedding Ag-NRs, the absorption of the reference active layer was broadened with a simultaneous increase in absorbance over a range of 350−800 nm until a Ag-NR concentration of 1 wt % was reached, followed by a reduction at 1.5 wt %. This increment is attributed to the LSPR of Ag-NRs, which is from 400 to 800 nm, as well as a scattering effect that broadened its absorbance above 700 nm.[20] It is worth noting that the effect of the rod-like shape of the Ag-NPs is the main reason for the broadening of the absorbance of the photoactive layer due to the multimode resonances along the longitudinal and transverse mode that extends its LSPR to the near-infrared region.[21] Interestingly, despite the fact that the NP aggregation at a high concentration (1.5% Ag-NR) prevented the enhancement of the absorption of the active layer around 500 nm,[22] there is a significant absorption increment over 700 nm when compared to that of the reference thin film. This result indicates the advantages of the rod-like shape over the commonly used spherical NPs to improve the absorbance of wide bandgap-based OSCs. Consequently, improved PCEs are expected in OSCs fabricated from wide-bandgap polymers in which optimized amounts of Ag-NRs are embedded.[23,24]

https://doi.org/10.1021/acsomega.3c08386
ACS Omega 2024, 9, 8082−8091

***J*–*V* Characteristics for OSC Devices.** To investigate the role of plasmonic enhancement in the performance of OSCs by Ag-NRs, devices with an inverted structure, i.e., ITO/ZnO/**PIDTT-BTz**:$PC_{71}BM$:Ag-NRs(%)/MoO_3/Al, were fabricated by embedding different concentrations of Ag-NRs (0, 0.5, 1, and 1.5 wt %) in the active layer. The molecular structures of the donor and acceptor materials as well as the device structure and energy levels are shown in Figure 2a–d. The *J*–*V* characteristics of the fabricated devices are shown in Figure 4b, while the corresponding photovoltaic (PV) parameters are summarized in Table 1. The PCE of the reference device (3.14%) was improved with the incorporation of Ag-NRs in the active layer, with the maximum at 1 wt % (PCE = 4.93%), revealing a 26% increment. The improvement in PCE with Ag-NRs is mainly due to the increased J_{SC}, as shown in Table 1, consistent with the increased and broader absorption of the active layer in which Ag-NRs are embedded (Figure 4a). However, the increment in J_{SC} was found to be maximum at the optimum concentration of 1 wt % Ag-NRs, which was found to decrease as the concentration was increased further to 1.5 wt %. This decrease might be a result of the formation of highly agglomerated NPs that might impede charge percolation, which could promote high charge-carrier recombination.[23,24] It should still be noted here that the J_{SC} value of the device in which 1.5 wt % Ag-NRs are embedded (12.21 mA/cm^2) is still higher than that of the reference device (11.92 mA/cm^2), mainly due to the improved light trapping by scattering.

Table 1. *J*–*V* Characteristics of the Fabricated OSCs at Different Amounts of Ag-NPs in the PIDTT-BTz: $PC_{71}BM$ Active Layer

Ag-NRs in the active layer (wt %)	V_{OC} (V)	J_{SC} (mA cm^{-2})	FF (%)	PCE (%)	R_s (Ω cm^2)
0	0.83	11.92	39.50	3.94	328.98
0.5	0.85	12.79	39.39	4.29	255.03
1	0.85	13.58	42.65	4.93	203.65
1.5	0.84	12.21	39.40	4.05	280.75

Furthermore, it can be noticed that in the improved plasmonic OSCs, the fill factor (FF) of the reference device increased from 39.50 to 42.65%. This is in agreement with the lower series resistance (R_S) in the plasmonic device compared with that of the reference. The open-circuit voltage (V_{OC}) of the devices, on the other hand, essentially stayed unaltered. Numerous studies have demonstrated that the efficiency of polymer solar cells depends on the energy difference between the highest occupied molecular orbital (HOMO) level of the donor polymer (**PIDTT-BTz**) and the lowest unoccupied molecular orbital (LUMO) level of the acceptor ($PC_{71}BM$) when the negative and positive electrodes are in Ohmic contact with the active layer. Therefore, it can be concluded that Ag-NRs did not change the structures of the active layer materials in a way that would have affected their energy levels.

Charge Generation and Transfer Kinetics. In order to further investigate the effect of Ag-NRs on optical absorption, we calculated the maximum photoinduced carrier generation rate (G_{max}) in devices with and without Ag-NRs. Figure 5b illustrates the relationship between photocurrent density (J_{ph}) and effective voltage (V_{eff}) for the reference and devices with embedded NPs. Here, $J_{ph} = J_L - J_D$, where J_L and J_D are the current density under illumination and in the dark, respectively, and $V_{eff} = V_o - V_a$, where V_o is the voltage when J_{ph} equals zero (i.e., $J_L = J_D$) and V_a is the applied voltage.[25−27] Apparently, J_{ph} increases linearly in the low V_{eff} range and saturates at high V_{eff}. Therefore, the values of the saturation photocurrent density (J_{sat}) can be calculated from Figure 5b and are summarized in Table 2. Then, G_{max} was obtained from $J_{ph} = qG_{max}L$, where q is the electron charge and L is the thickness of the active layer. The values of G_{max} for the reference and devices with 1% Ag-NRs were 8.35×10^{21} cm^{-3} s^{-1} (J_{sat} = 13.32 mA cm^{-2}) and 9.06×10^{21} cm^{-3} s^{-1} (J_{sat} = 14.50 mA cm^{-2}), respectively. Thus, a considerable improvement in G_{max} occurred after incorporating 1 wt % Ag-NRs into the active layer.

As the value of G_{max} is related to the maximum absorption of incident photons,[28,29] the increase of G_{max} suggests enhanced light absorption in the device with Ag-NRs embedded in the active layer, which is consistent with the result of the absorption spectra of the active layer (Figure 4a). Once the excitons are generated in the active layer, they need to be dissociated into free carriers and collected through the electrodes to generate photocurrent. Hence, the exciton dissociation probabilities ($P(E,T)$) and charge collection

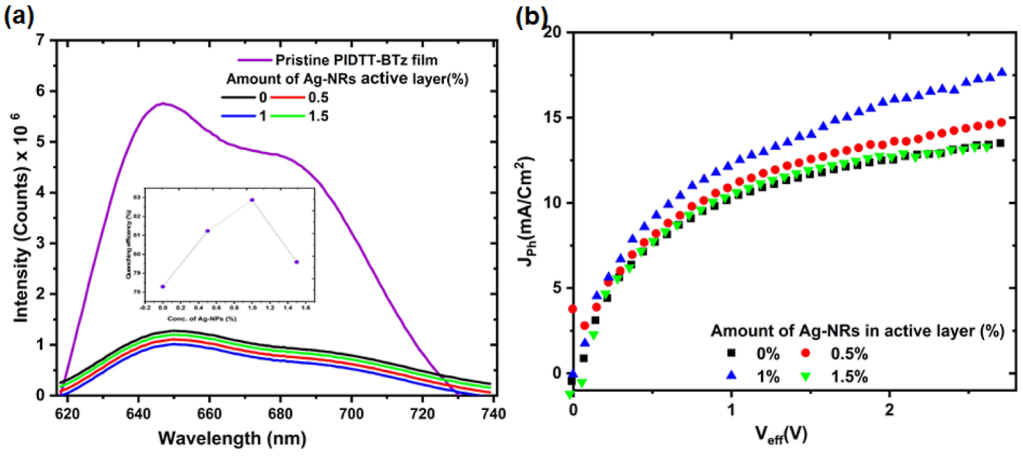

Figure 5. (a) PL spectra of active films with different concentrations of Ag-NRs in the active layer (inset: the comparison of quenching efficiency (QE)) (b) Photocurrent density (J_{ph}) as a function of the effective voltage (V_{eff}) for control and doped devices under constant incident light intensity.

https://doi.org/10.1021/acsomega.3c08386
ACS Omega 2024, 9, 8082−8091

Table 2. J_{ph}, J_{sat}, G_{max}, $P(E,T)$, and QE of OSC Devices Made from the Active Layer Embedded with Different Concentrations of Ag-NRs

Ag-NRs in the active layer (wt %)	QE (%)	J_{ph} (mA cm^{-2})	J_{sat} (mA cm^{-2})	G_{max} (s^{-1} cm^{-3}) × 10^{21}	$P(E,T)$ (%)
0	78.28	11.92	13.32	8.35	89.48
0.5	81.23	12.79	13.98	8.75	91.48
1	82.86	13.58	14.50	9.06	93.65
1.5	79.59	12.21	13.52	8.45	90.31

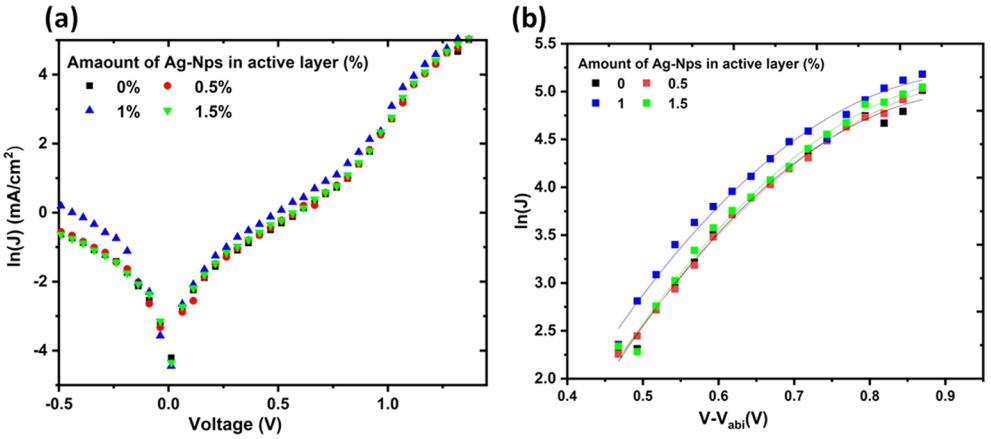

Figure 6. (a) $J-V$ characteristics under the dark condition; (b) charge mobility fitted with the Mott−Gurney law for reference and different concentrations of Ag-NRs in the active layer.

probabilities (CP) for the solar cells were compared at a constant electric field (E) and temperature (T). For polymer solar cells, only a portion of photogenerated excitons can dissociate into free carriers. Therefore, J_{ph} can be expressed using the equation $J_{ph} = qG_{max}P(E,T)L$. The value of $P(E,T)$ at any bias can be obtained by normalizing photocurrent density with the J_{SC} (J_{ph}/J_{sat}).[30] Table 2 shows that the value of $P(E,T)$ increased from 89.48% (for the reference device) to 93.65% (for the optimal device) under short-circuit conditions (V_a = 0 V), indicating that the excitation of LSPR by Ag-NRs facilitated excitons to dissociate into free carriers. Hence, the J_{SC} of the solar cell with plasmonic Ag-NRs embedded in the active layer was improved as a result of the LSPR's excitation by increasing both the exciton generation rate and the dissociation probability. To further investigate the exciton dissociation in the active layers, steady-state photoluminescence (PL) spectra with an excitation at 510 nm were recorded. The relaxation of excitons generated by the excitation of electrons from the HOMO to the LUMO of the polymer is the cause of the PL of the pristine **PIDTT-BTz**. When the polymer is blended with $PC_{71}BM$, the electron in the LUMO of excited **PIDTT-BTz** will be transferred to the LUMO of $PC_{71}BM$, leaving the hole in the HOMO of the donor. As a result, the emission expected from the relaxation of excitons of the donor will be greatly quenched, allowing for the direct calculation of exciton QE, where QE = 1 − $PL_{blend}/PL_{pristine}$.[31] The PL spectra of **PIDTT-BTz**:$PC_{71}BM$ films without and with Ag-NRs are shown in Figure 5a. Doping with Ag-NRs increases the PL quenching in the active layer with the maximum at 1% Ag-NRs compared to that of the reference film, which indicates improved exciton dissociation assisted by Ag-NRs, consistent with the probability of dissociation (Table 2).

Charge Transport Properties in OSCs. An important aspect of understanding the electrical properties of polymer solar cells is the charge transport process. In thin-film OSCs, space-charge-limited current (SCLC) creates a conducive environment for studying the charge transport properties across the photoactive layer. The dark-current of the device grows from an injection-limited regime below 1 V to an SCLC regime, which grows into a saturation point with a further increase in the applied voltage, as shown in Figure 6a. The SCLC was then fitted with the field-dependent mobility equation (eq 1) used in Mott−Gurney's law.[32,33]

$$J_{SCLC} = \frac{9}{8}\varepsilon\varepsilon_o\mu_o\frac{V^2}{L^3}\exp\left(\gamma 0.86\sqrt{\frac{V}{L}}\right) \quad (1)$$

where V and L (100 nm) stand for the applied voltage corrected for built-in voltage (V_b) and the photoactive layer's thickness of the device, respectively. ε = 3 and ε_o = 8.854 × 10^{-12} F/m are the dielectric constant of the photoactive layer and the free space permittivity, respectively, while μ_o and γ are the zero-field mobility and field activation factors, respectively. It should be noted that recent studies indicate that the mobility of polymer solar cells decreases at large applied electric fields due to the negative values found at the field activation factor.[34]

The fitting results of the SCLC are displayed in Figure 6b, and the results are summarized in Table 3. The results demonstrate that the zero-field mobility of the reference device was almost doubled when the optimum concentration of Ag-NRs (1%) was embedded in the active layer. The better charge

Table 3. Space Charge Mobility and the Field Activation Factor Extracted from SCLC Fit

Ag-NRs in the active layer (%)	μ_0 (×cm^2 V^{-1} s $^{-1}$)10^{-3})	γ (×10^{-4}(cm/V)$^{1/2}$
0	1.23	−6.10
0.5	1.30	−6.42
1	2.31	−8.62
1.5	1.23	−6.15

https://doi.org/10.1021/acsomega.3c08386
ACS Omega 2024, 9, 8082−8091

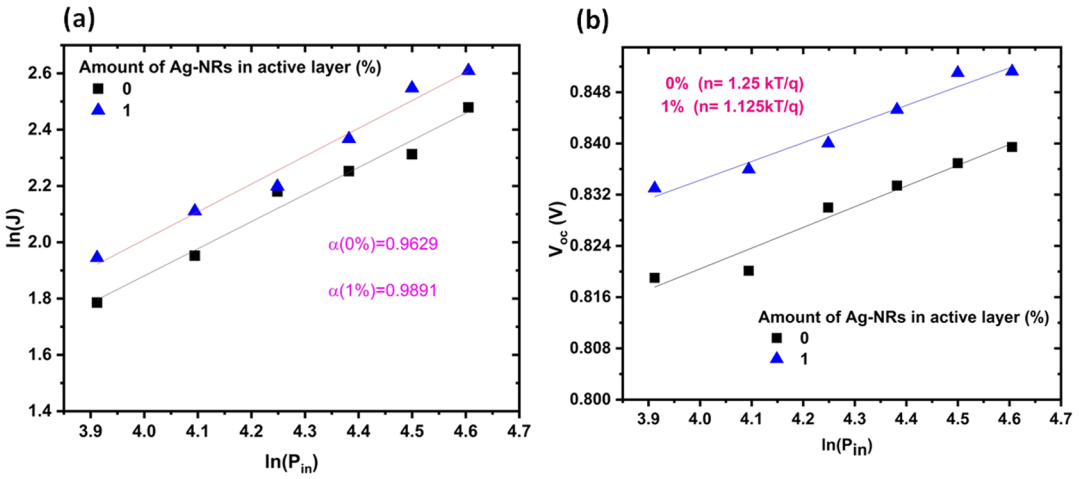

Figure 7. (a) J_{SC} dependence on the incident light intensity of the OSCs. (b) V_{OC} dependence on the incident light intensity of the OSCs.

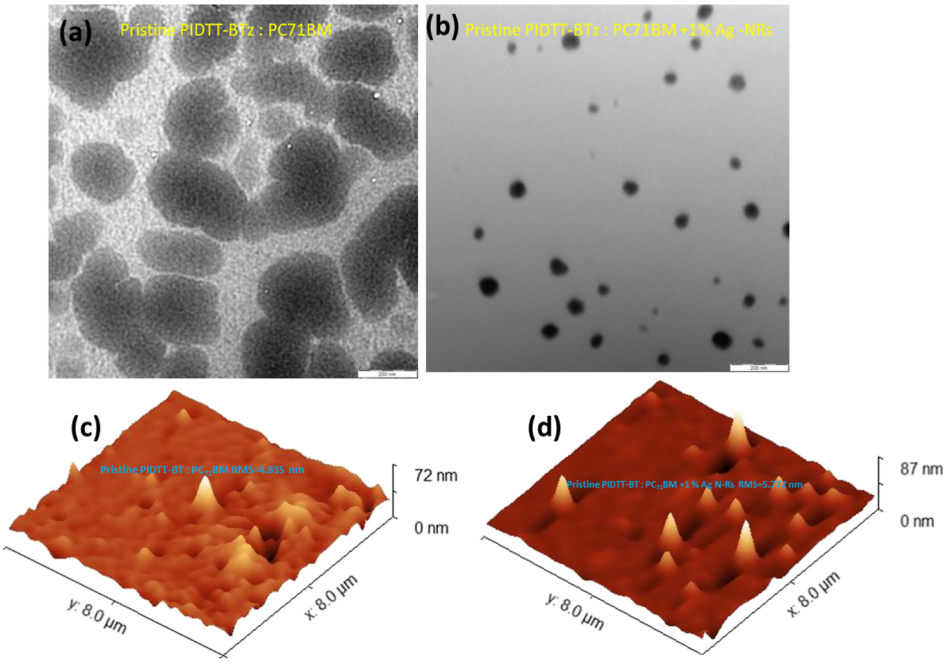

Figure 8. TEM image of the active layer (a) without Ag-NRs and (b) with 1 wt % Ag-NRs and AFM image of the active layer (c) without Ag-NRs and (b) with 1 wt % Ag-NRs.

transport in the optimized plasmonic device is expected to facilitate charge transport, and thus, the improvement in the current can also be attributed to an increase in effective charge mobility. Furthermore, because the traps are filled at low electric fields, the field activation factor in the optimized plasmonic device was found to be the lowest, indicating less field dependence on the mobility to achieve SCLC.

Recombination Kinetics. The $J-V$ curves of the reference and optimized plasmonic devices at different light illumination intensities were recorded to obtain more insight into the charge recombination kinetics. The dependence of J_{SC} and V_{OC} on the light intensity of the reference device and devices with an optimal concentration of Ag-NRs in the active layer are depicted in Figure 7a,b, respectively. The charge recombination in the devices can be determined from the slope of the J_{SC} *vs* incident light intensity (P_{in}) curve plotted in a double logarithmic scale, which follows a power law ($J_{SC} \propto P_{in}^{\alpha}$) where α is below 1, indicating the presence of bimolecular recombination of charge carriers.[35] The values of α in OSCs with 0 and 1 wt % Ag-NRs in the active layer were 0.96 and 0.99, respectively, confirming that embedding Ag-NRs can partially inhibit bimolecular recombination, which is consistent with the increased J_{SC} of the device with 1 wt % Ag-NRs. Moreover, the slope of the V_{OC} *vs* $\ln(P_{in})$ curve is close to kT/q, suggesting that bimolecular recombination is dominant.[35] From Figure 7b, the slopes of the curves for the devices without and with 1 wt % Ag-NRs in the active layer were calculated to be 1.25 and 1.12 kT/q, respectively. This indicates that the addition of 1 wt % Ag-NRs in the **PIDTT-BTz**:$PC_{71}BM$ active layer suppressed the trap-induced charge recombination as compared to the reference device.

Morphological and Raman Investigation. The active layer morphology of an OSC is a crucial parameter that determines its photogeneration processes. An optimized OSC is expected to have a morphology with a good interpenetrating network of the donor and acceptor materials to efficiently

https://doi.org/10.1021/acsomega.3c08386
ACS Omega 2024, 9, 8082−8091

dissociate excitons while maintaining a percolation path of interconnected donor and acceptor units for charge transport.[36] The active layer morphology of the **PIDTT-BTz**:$PC_{71}BM$ blend and the optimized plasmonic devices were analyzed by using TEM, as shown in Figure 8. The reference device reveals interpenetrating phases of $PC_{71}BM$, as depicted by the black images, due to its higher density (1.5 g/cm^3)[37] compared to that of the polymer. It is also evident that the volume fraction of $PC_{71}BM$ in the active layer was higher but still dispersed within the polymer. The TEM image of the optimized plasmonic device with 1% Ag-NRs (Figure 8) reveals that the NPs are well-dispersed within the polymer−fullerene matrix. This is crucial as the aggregation of the NPs might serve as a recombination center, impeding charge photogeneration. Hence, the active layer morphology of the **PIDTT-BTz**:$PC_{71}BM$:1% Ag-NR plasmonic device does not inhibit charge generation. Additionally, the atomic force microscopy (AFM) images of the active layer shown in Figure 8c,d were used to determine the surface morphology of the layer. It was discovered that the pristine and Ag-NR-incorporated active layers had corresponding roughness values of 4.83 and 5.78 nm, respectively. Ag-NR inclusion is expected to cause a minor increase in the active layer's roughness; nevertheless, as the TEM pictures showed, the NRs do not form significant aggregates that will lower charge generation.

Moreover, the effect of Ag-NRs on the molecular ordering of the active layer materials was monitored by their Raman spectra, as shown in Figure 9. Raman peaks at 760, 973.2,

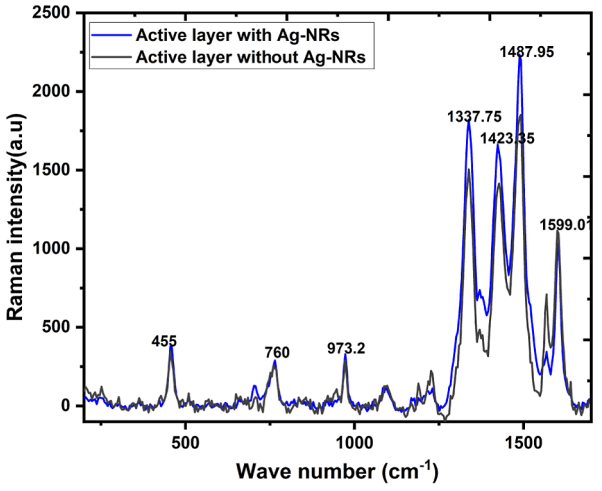

Figure 9. Raman spectra of active layer films without and with 1% Ag-NRs.

1337.75, 1423.35, and 1487.95 cm^{-1} corresponding to the vibrational modes of C−S−C ring deformation in thiophene rings, a combination of C−C stretching and C−H stretching mode, C−C intraring stretch mode, and C═C stretch mode in thiophene, respectively, were observed in the spectrum of the reference **PIDTT-BTz**:$PC_{71}BM$ BHJ film. The Raman bands observed in the spectrum of the active layer in which Ag-NRs are embedded are similar to those of the reference, confirming that there is no structural modification of the active layer materials by the NPs. The high-frequency Raman modes were enhanced upon incorporation of Ag-NRs, while the modes at 760 and 973.2 cm^{-1} remained unchanged. This is because excitation of the LSPR of the Ag-NRs is expected to enhance Raman scattering intensity through surface-enhanced Raman scattering (SERS), which is beneficial for trapping the incoming light in the device.[38] In summary, the similar Raman modes in the reference and plasmonic devices confirmed the intact conformation of the active layer material with the incorporation of the Ag-NRs. Furthermore, enhanced scattering indicated by a higher intensity in the high-frequency Raman modes due to SERS is expected to increase the light trapping in the device by multiple scattering. Finally, the TEM images revealed well-dispersed Ag-NRs, maintaining a good morphology of the active layer, while the Raman spectrum showed a higher level of light trapping in the plasmonic device. Consequently, enhanced J_{SC} in the plasmonic device is expected due to the better light scattering efficiency.

CONCLUSIONS

In summary, we studied the photovoltaic performances of the wide-bandgap polymer **PIDTT-BTz** and improved the PCE of **PIDTT-BTz**:$PC_{71}BM$-based OSCs by incorporating Ag-NRs into the active layer. As a result of LSPR-induced local field enhancement, the active layer material absorbs more light, and charge separation and transport are improved, resulting in enhanced J_{SC}, FF, and PCE. These improvements are caused by enhanced optical absorption due to LSPR, combined with light scattering. Furthermore, high-conductivity Ag-NRs resulted in low R_s values because they increased carrier mobility. As a result, a high PCE of 4.9% with an improvement of 26% was achieved from the device in which 1% Ag-NRs were embedded as compared to that of the device without the Ag-NRs. In thin-film OSCs, such improvements result from LSPR and far-field scattering, which enhance light trapping, exciton dissociation, and charge transport processes. We believe that this is a promising approach for improving the efficiencies of OSC devices, which may stimulate future research on solar cells.

AUTHOR INFORMATION

Corresponding Authors

Alemayehu G. Waketola − *Department Physics Education, Kotebe University of Education, Addis Ababa 31248, Ethiopia; Department of Physics, Addis Ababa University, Addis Ababa 1176, Ethiopia;* orcid.org/0009-0008-5303-4462; Phone: +251913456107; Email: alemayehugirma27@gmail.com

Newayemedhin A. Tegegne − *Department of Physics, Addis Ababa University, Addis Ababa 1176, Ethiopia;* orcid.org/0000-0002-5822-9145; Phone: +251912103048; Email: newaye.medhin@aau.edu.et

Authors

Fekadu G. Hone − *Department of Physics, Addis Ababa University, Addis Ababa 1176, Ethiopia*

Fikadu T. Geldasa − *Department of Applied Physics, Adama Science and Technology University, Adama 302120, Ethiopia*

Zewdneh Genene − *Department of Chemistry and Chemical Engineering, Chalmers University of Technology, Goteborg SE412 96, Sweden*

Wendimagegn Mammo − *Department of Chemistry, Addis Ababa University, Addis Ababa 33658, Ethiopia*

Complete contact information is available at: https://pubs.acs.org/10.1021/acsomega.3c08386

https://doi.org/10.1021/acsomega.3c08386
ACS Omega 2024, 9, 8082−8091

Notes

The authors declare no competing financial interest.

■ ACKNOWLEDGMENTS

We would like to thank the International Science Program (ISP) of Uppsala University, Sweden, for funding the polymer physics laboratory at Addis Abeba University. WM and ZG would also like to acknowledge ISP for financial support. We would also like to thank Prof. Tame Mark and Jane Dai for the AFM images.

■ REFERENCES

(1) Chuang, M.-K.; Chen, F.-C. Synergistic plasmonic effects of metal nanoparticle−decorated PEGylated graphene oxides in polymer solar cells. *ACS Appl. Mater. Interfaces* **2015**, *7*, 7397−7405.
(2) Bao, Z. Y.; Liu, S.; Hou, Y.; Shang, A.; Yan, F.; Wu, Y.; Lei, D.; Dai, J. Hollow Au nanorattles for boosting the performance of organic photovoltaics. *J. Mater. Chem. A* **2019**, *7*, 26797−26803.
(3) Wang, Y.; Zheng, Z.; Wang, J.; Liu, X.; Ren, J.; An, C.; Zhang, S.; Hou, J. New Method for Preparing ZnO Layer for Efficient and Stable Organic Solar Cells. *Adv. Mater.* **2023**, *35*, 2208305.
(4) Wang, X.; Wang, J.; Wang, P.; Han, C.; Bi, F.; Wang, J.; Zheng, N.; Sun, C.; Li, Y.; Bao, X. Embedded Host/Guest Alloy Aggregations Enable High-Performance Ternary Organic Photovoltaics. *Adv. Mater.* **2023**, *35*, 2305652.
(5) Han, C.; Wang, J.; Zhang, S.; Chen, L.; Bi, F.; Wang, J.; Yang, C.; Wang, P.; Li, Y.; Bao, X. Over 19% efficiency organic solar cells by regulating multidimensional intermolecular interactions. *Adv. Mater.* **2023**, *35*, 2208986.
(6) Scharber, M. C.; Sariciftci, N. S. Efficiency of bulk-heterojunction organic solar cells. *Prog. Polym. Sci.* **2013**, *38*, 1929−1940.
(7) Hedley, G. J.; Ruseckas, A.; Samuel, I. D. Light harvesting for organic photovoltaics. *Chem. Rev.* **2017**, *117*, 796−837.
(8) Waketola, A. G.; Hone, F. G.; Mola, G. T.; Oseni, S. O.; Ogutu, H.; Tegegne, N. A. Hybrid silver/silver-oxide nanoparticles doped hole transport layer for efficient photon harvesting in organic solar cells. *Appl. Phys. A: Mater. Sci. Process.* **2023**, *129*, 96.
(9) Heidarzadeh, H. Effect of parasitic absorption of the plasmonic cubic nanoparticles on the performance of a plasmonic assisted halide thin-film perovskite solar cell. *Sol. Energy* **2021**, *223*, 293−301.
(10) Trendafilov, S.; Allen, M.; Allen, J.; Lin, Z. Comparison of Octahedral and Spherical Nanoparticles for Plasmonics. *IEEE Photonics J.* **2019**, *11*, 1−6.
(11) Rekha, C.; Nayar, V.; Gopchandran, K. Synthesis of highly stable silver nanorods and their application as SERS substrates. *J. Sci.: Adv. Mater. Devices* **2018**, *3*, 196−205.
(12) Hsiao, Y.-S.; Charan, S.; Wu, F.-Y.; Chien, F.-C.; Chu, C.-W.; Chen, P.; Chen, F.-C. Improving the light trapping efficiency of plasmonic polymer solar cells through photon management. *J. Phys. Chem. C* **2012**, *116*, 20731−20737.
(13) Spyropoulos, G. D.; Stylianakis, M. M.; Stratakis, E.; Kymakis, E. Organic bulk heterojunction photovoltaic devices with surfactant-free Au nanoparticles embedded in the active layer. *Appl. Phys. Lett.* **2012**, *100*, 213904.
(14) Rivera-Taco, J.; Castro-Beltrán, R.; Maldonado, J.-L.; Álvarez-Martínez, J.; Barreiro-Argüelles, D.; Gaspar, J. A.; Gutiérrez-Juárez, G. The role of silver nanoparticles in the hole transport layer in organic solar cells based on PBDB-T: ITIC. *J. Electron. Mater.* **2021**, *50*, 4118−4127.
(15) Lin, Y.; Fan, H.; Li, Y.; Zhan, X. Thiazole-based organic semiconductors for organic electronics. *Adv. Mater.* **2012**, *24*, 3087−3106.
(16) Guo, B.; Li, W.; Guo, X.; Meng, X.; Ma, W.; Zhang, M.; Li, Y. A novel wide bandgap conjugated polymer (2.0 eV) based on bithiazole for high efficiency polymer solar cells. *Nano Energy* **2017**, *34*, 556−561.
(17) Negash, A.; Genene, Z.; Eachambadi, R. T.; Verstappen, P.; Van den Brande, N.; Kesters, J.; D'Haen, J.; Wang, E.; Vandewal, K.; Maes, W.; et al. Ladder-type high gap conjugated polymers based on indacenodithieno [3, 2-b] thiophene and bithiazole for organic photovoltaics. *Org. Electron.* **2019**, *74*, 211−217.
(18) Singh, S.; Bharti, A.; Meena, V. K. Green synthesis of multi-shaped silver nanoparticles: Optical, morphological and antibacterial properties. *J. Mater. Sci.: Mater. Electron.* **2015**, *26*, 3638−3648.
(19) Bhoomanee, C.; Ruankhama, P.; Choopun, S.; Prathan, A.; Wongratanaphisan, D. Effect of al-doped ZnO for electron transporting layer in planar perovskite solar cells. *Mater. Today: Proc.* **2019**, *17*, 1259−1267.
(20) Baek, S.-W.; Noh, J.; Lee, C.-H.; Kim, B.; Seo, M.-K.; Lee, J.-Y. Plasmonic forward scattering effect in organic solar cells: a powerful optical engineering method. *Sci. Rep.* **2013**, *3*, 1726.
(21) Liu, C.; Zhao, C.; Zhang, X.; Guo, W.; Liu, K.; Ruan, S. Unique gold nanorods embedded active layer enabling strong plasmonic effect to improve the performance of polymer photovoltaic devices. *J. Phys. Chem. C* **2016**, *120*, 6198−6205.
(22) Hu, G.; Liang, G.; Zhang, W.; Jin, W.; Zhang, Y.; Chen, Q.; Cai, Y.; Zhang, W. Silver nanoparticles with low cytotoxicity: controlled synthesis and surface modification with histidine. *J. Mater. Sci.* **2018**, *53*, 4768−4780.
(23) Chow, P. C.; Gélinas, S.; Rao, A.; Friend, R. H. Quantitative bimolecular recombination in organic photovoltaics through triplet exciton formation. *J. Am. Chem. Soc.* **2014**, *136*, 3424−3429.
(24) Ahmed, A. Y.; Ike, J. N.; Hamed, M. S.; Mola, G. T. Silver decorated magnesium doped photoactive layer for improved collection of photo-generated current in polymer solar cell. *J. Appl. Polym. Sci.* **2023**, *140*, No. e53697.
(25) Shuttle, C.; Hamilton, R.; O'Regan, B. C.; Nelson, J.; Durrant, J. Charge-density-based analysis of the current−voltage response of polythiophene/fullerene photovoltaic devices. *Proc. Natl. Acad. Sci. U.S.A.* **2010**, *107*, 16448−16452.
(26) Cowan, S. R.; Roy, A.; Heeger, A. J. Recombination in polymer-fullerene bulk heterojunction solar cells. *Phys. Rev. B: Condens. Matter Mater. Phys.* **2010**, *82*, 245207.
(27) Lu, H.; Xu, X.; Bo, Z. Perspective of a new trend in organic photovoltaic: ternary blend polymer solar cells. *Sci. China Mater.* **2016**, *59*, 444−458.
(28) Hao, Y.; Song, J.; Yang, F.; Hao, Y.; Sun, Q.; Guo, J.; Cui, Y.; Wang, H.; Zhu, F. Improved performance of organic solar cells by incorporating silica-coated silver nanoparticles in the buffer layer. *J. Mater. Chem. C* **2015**, *3*, 1082−1090.
(29) Babaei, Z.; Rezaei, B.; Pisheh, M. K.; Afshar-Taromi, F. In situ synthesis of gold/silver nanoparticles and polyaniline as buffer layer in polymer solar cells. *Mater. Chem. Phys.* **2020**, *248*, 122879.
(30) Zang, Y.; Cao, K.-l.; Huang, J.; Zhang, Q.; Yu, J.-s. Significant Enhancement in Built-in Potential and Charge Carrier Collection of Organic Solar Cells using 4-(5-hexylthiophene-2-yl)-2, 6-bis (5-trifluoromethyl) thiophen-2-yl) pyridine as a Cathode Buffer Layer. *Chin. J. Chem. Phys.* **2014**, *27*, 593−599.
(31) Ding, G.; Chen, T.; Wang, M.; Xia, X.; He, C.; Zheng, X.; Li, Y.; Zhou, D.; Lu, X.; Zuo, L.; et al. Solid Additive-Assisted Layer-by-Layer Processing for 19% Efficiency Binary Organic Solar Cells. *Nano-Micro Lett.* **2023**, *15*, 92.
(32) Zhang, X.-G.; Pantelides, S. T. Theory of space charge limited currents. *Phys. Rev. Lett.* **2012**, *108*, 266602.
(33) Yang, M.; Fu, S.; Wang, L.; Ren, M.; Li, H.; Han, S.; Lu, X.; Lu, F.; Tong, J.; Li, J. Efficient organic solar cells by modulating photoactive layer morphology with halogen-free additives. *Opt. Mater.* **2023**, *137*, 113503.
(34) Mohammed, Y. A.; Hone, F. G.; Mola, G. T.; Tegegne, N. A. The roles of acceptors in the thermal-degradation of P3HT based organic solar cells. *Phys. B* **2023**, *653*, 414666.
(35) Kong, T.; Wang, R.; Zheng, D.; Yu, J. Modification of the SnO2 electron transporting layer by using perylene diimide derivative for efficient organic solar cells. *Front. Chem.* **2021**, *9*, 703561.

https://doi.org/10.1021/acsomega.3c08386
ACS Omega 2024, 9, 8082−8091

(36) Xu, X.; Li, Y.; Peng, Q. Ternary blend organic solar cells: understanding the morphology from recent progress. *Adv. Mater.* **2022**, *34*, 2107476.
(37) Sun, Y.; Han, Y.; Liu, J. Controlling PCBM aggregation in P3HT/PCBM film by a selective solvent vapor annealing. *Chin. Sci. Bull.* **2013**, *58*, 2767−2774.
(38) Stavytska-Barba, M.; Salvador, M.; Kulkarni, A.; Ginger, D. S.; Kelley, A. M. Plasmonic enhancement of Raman scattering from the organic solar cell material P3HT/PCBM by triangular silver nanoprisms. *J. Phys. Chem. C* **2011**, *115*, 20788−20794.

https://doi.org/10.1021/acsomega.3c08386
ACS Omega 2024, 9, 8082−8091